**Preprint of:** Blocken B, Poesen J, Carmeliet J. 2006. Impact of wind on the spatial distribution of rain over micro-scale topography – numerical modelling and experimental verification.
Hydrological Processes 20(2): 345-368 (doi:10.1002/hyp.5865) © Wiley.

# Impact of wind on the spatial distribution of rain over micro-scale topography - numerical modelling and experimental verification

Bert Blocken[1]*, Jean Poesen[2] and Jan Carmeliet[1,3]

[1] *Department of Civil Engineering, Laboratory of Building Physics, K.U.Leuven, Kasteelpark Arenberg 40, 3001 Leuven, Belgium*
[2] *Laboratory for Experimental Geomorphology, K.U.Leuven, Redingenstraat 16, 3000 Leuven, Belgium*
[3] *Faculty of Building and Architecture, Building Physics Group, T.U.Eindhoven, P.O. box 513, 5600 MB Eindhoven, The Netherlands*

*Author to whom correspondence should be addressed
Tel.: +32 (0) 16 32 13 45
Fax: +32 (0) 16 32 19 80
E-mail: bert.blocken@bwk.kuleuven.be

Abstract:

The wind-driven-rain effect refers to the redistribution of rainfall over micro-scale topography due to the existence of local perturbed wind-flow patterns. Rainfall measurements reported in the literature point to the fact that the wind-driven-rain distribution can show large variations over micro-scale topography. These variations should be taken into account in hillslope hydrology, in runoff and erosion studies and in the design of rainfall monitoring networks. In practice, measurements are often not suitable for determining the wind-driven-rain distribution. Therefore, a few researchers have employed numerical modelling. In order to provide confidence in using numerical models, experimental verification for a range of different topographic features is imperative. The objective of this study is to investigate the adequacy of a 2-dimensional Computational Fluid Dynamics (CFD) model to predict the wind-driven-rain distribution over micro-scale topography. The numerical model is applied to a number of topographic features including a succession of cliffs, a small isolated hill, a small valley and a field with ridges and furrows. The numerical results are compared with the corresponding measurement results reported in the literature. It is shown that 2-dimensional numerical modelling can provide a good indication of the wind-driven-rain distribution over each type of micro-scale topography that is considered in this study. It is concluded that more detailed verification procedures are currently inhibited due to the lack of available and detailed spatial and temporal rainfall data from field measurements.

KEY WORDS wind-driven rain; driving rain; meteorological rain, hydrological rain, rainfall distribution; micro-scale topography; Computational Fluid Dynamics; numerical simulation

## INTRODUCTION

The term wind-driven-rain (WDR) effect refers to the interaction between wind, rain and micro-scale topographical features. When the wind blows over small hills, valleys, cliffs or ridges, specific wind-flow patterns develop in the vicinity of these configurations. Raindrops, when entering these patterns, will be driven by the local wind vectors (wind-driven rain) and will be redistributed in a specific pattern. This

effect can lead to very large rainfall gradients and should therefore be adequately included in rainfall and rainfall-related studies. The WDR effect has to be distinguished from the orographic effect. Both effects influence the rainfall distribution, but the orographic effect acts on larger scales (meso-scale). The orographic effect refers to the forced uplifting of air masses as they are moving over mountains and is responsible for the increase of rainfall with elevation in mountainous areas.

Information about the WDR effect over micro-scale topography is important in a number of research areas including earth sciences, agriculture and meteorology. Knowledge of the WDR distribution is important for catchment hydrology (Sharon, 1970), (Reid, 1973), for runoff and erosion studies (Sharon *et al.*, 1983), (Poesen, 1986; 1988), (Sharon *et al.* 1988), (Erpul, 2001), (Erpul *et al.*, 2002; 2003a; 2003b), for the determination of cropping conditions, for studies of the topographic distribution of forest-fire danger (Hayes, 1944) and for the design of rainfall monitoring networks (Hutchinson, 1970). WDR distribution conditions determine the representativeness of point rain measurements on hill slopes (Pagliuca, 1934), (Fourcade, 1942), (Hayes, 1944), (Hamilton, 1954), (Sandsborg, 1970), (Sharon, 1980), (de Lima, 1990), near buildings (Lacy, 1951) and near trees or other obstructions (Hayes and Kittredge, 1949). The correct inclusion of the WDR effect as a boundary condition in erosion studies is imperative as the obliquity and increased kinetic energy of rainfall influences processes such as soil detachment and can cause raindrop splash anisotropy and upslope splash drift (Van Heerden, 1964), (Lyles *et al.*, 1969), (Disrud, 1970), (Disrud and Krauss, 1971), (Lyles *et al.*, 1974), (Moeyersons and De Ploey, 1976), (Lyles, 1977), (Lal *et al.*, 1980), (Jungerius *et al.*, 1981), (Moeyersons, 1983), (Poesen, 1985; 1986; 1988), (de Lima, 1989), (Jungerius and Dekker, 1990), (de Lima *et al.*, 1992), (Van Dijk *et al.*, 1996), (Gabriëls *et al.*, 1997), (Goossens *et al.* 2000), (Erpul, 2001), (Erpul *et al.*, 2002; 2003a; 2003b). WDR can also play an important role in rainfall interception by plants (comments by Fourcade (1942) on Phillips (1926, 1928)) and in spore removal and spreading of plant diseases (McManus and Jones, 1994), (Sache, 2000).

Three methods are available to study the WDR effect over micro-scale topography: (1) rainfall measurements over natural topography, (2) measurements over artificial topography and (3) numerical modelling. Most researchers have employed the first method (James, 1964), (Geiger, 1965), (Hovind, 1965), (Sandsborg, 1970), (Sharon, 1970), (Reid, 1973), (Sharon, 1980), (Craig, 1980), (Sharon *et al.*, 1983; 1988), (Sharon and Arazi, 1997). These measurements have been the primary tool to identify the WDR effect and have provided a considerable amount of knowledge about this phenomenon. Drawbacks however are that measurements are expensive, time-consuming and often not feasible in practice. To bypass some of the typical drawbacks of measurements on natural topography, Lentz *et al.* (1995) constructed a full-sized replica of a hill that could be moved and positioned at any location, with adjustable slope and summit elevation (length about 14 m, width 6 m, height adjustable from 1 to 3 m). This apparatus was designed to automatically maintain a windward orientation during precipitation events, thus reducing the time needed to obtain a number of relevant measurements. The limitations of using this type of artificial hill however are the high construction cost and the fact that it is not really representative of a real situation, because of its limited width and – in the case of the hill replica by Lentz (1995) - because wind could also flow sideways under the construction instead of only above and around it. Furthermore, the obtained results are only valid for the specific geometry that was tested. To overcome the drawbacks of the measurement approaches, some researchers have attempted numerical modelling. It consists of constructing a model of the topography, obtaining an estimate for the wind-flow pattern over it and calculating raindrop trajectories in this flow pattern. Based on the configurations of the trajectories, predictions of the hydrological rainfall intensity are obtained. The first numerical modelling efforts were made by Poreh and Mechrez (1984) and by Bradley *et al.* (1997). Poreh and Mechrez (1984) used analytical expressions for the wind field, whereas the latter adopted a simple potential flow model. Full numerical modelling was first performed by Arazi *et al.* (1997), and later by Choi (2002) and by Blocken *et al.* (2004). Full numerical modelling refers to the use of numerical techniques to solve the wind-flow field, i.e. solving the complex Reynolds-Averaged Navier-Stokes equations with Computational Fluid Dynamics (CFD).

Full numerical modelling, as opposed to analytical wind-flow expressions and potential flow models, offers the possibility of more accurate results and much more flexibility to study different topographical configurations. The accuracy of the results is to a large extent determined by the performance of the turbulence model in the CFD numerical procedure. The turbulence model is needed to model the effect of turbulence on the mean flow characteristics. The suitability of a turbulence model to be used for a specific type of flow problem is typically checked by comparing numerical simulations for this type of flow problem with corresponding experimental data. Therefore, in order to use numerical modelling with confidence for a wide range of topographies, experimental verification for an identically wide range of

topographies is needed. To our knowledge, the only experimental verification of full numerical modelling has been performed by Arazi *et al.* (1997). These authors have compared numerical results of the WDR distribution in a small valley with the corresponding detailed measurement data of Sharon and Arazi (1997), finding a good qualitative agreement.

The objective of this study is to investigate the adequacy of 2-dimensional numerical modelling to predict the WDR distribution over different micro-scale topographic configurations. The numerical model that will be used has been described elsewhere (Blocken *et al.*, 2004). This model is applied to predict the WDR distribution over (a) a succession of cliffs, (b) a small isolated hill, (c) a small valley and (d) a cultivated field with ridges and furrows. The numerical predictions are compared with measured rainfall patterns that have been published in the literature. Before describing the modelling exercise, first a brief review of the numerical model is given.

## NUMERICAL MODEL

In this section, only the main issues of the numerical model will be given. For more details, the reader is referred to (Blocken *et al.*, 2004). First the influencing parameters of WDR are defined. Next, the model itself is described and a number of important modelling considerations are highlighted.

*Definitions and parameters*

The WDR intensity falling over micro-scale topography is a complicated function of space and time. The six basic influencing parameters are: (1) the geometry of the topographic feature (including the geometry of the surroundings), (2) the position on the topography, (3) the reference wind speed, (4) the reference wind direction, (5) the reference rain intensity and (6) the raindrop-size distribution. The reference wind speed is defined as the horizontal component of the wind-velocity vector, situated outside the wind-flow pattern that is disturbed by the topography. It is indicated by $U_h$ where h is the height above ground at which the wind speed is given. The reference wind direction refers to the direction of the reference wind speed (degrees from north). The reference rain intensity refers to the meteorological rainfall, i.e. the rainfall intensity as measured by a conventional rain gauge with a horizontal orifice, per unit orifice area. In general, meteorological rainfall can refer to the standard reference rainfall as measured at weather stations (on level ground sufficiently far away from any obstructions) (Figure 1a) or to the rainfall measured on hill slopes (Figure 1b). In this paper, the term reference rainfall will be used to indicate the former type, i.e. the reference meteorological rainfall. It is indicated by R (rainfall rate or intensity in L/m²h or mm/h) or by S (rainfall sum or amount in L/m² or mm).

The WDR intensity or sum usually refers to the hydrological rainfall, i.e. the rainfall as it would be measured by a tilted rain gauge with its orifice parallel to the soil surface, per unit of horizontally projected orifice area (Figure 1c). It is indicated by R* and S* respectively. In the numerical model and in the verification procedure, the hydrological rainfall will be expressed in terms of dimensionless quantities, i.e. the specific catch ratio and the catch ratio. The specific catch ratio ($\eta_d$) is defined as the ratio of the hydrological rainfall intensity to the reference rainfall intensity for one specific raindrop diameter:

$$\eta_d(d,t) = \frac{R^*(d,t)}{R(d,t)} \tag{1}$$

where d is the raindrop diameter and t the time. The catch ratio ($\eta$) is defined in the same way, but now referring to all raindrop diameters (Eq. 2).

$$\eta(t) = \frac{R^*(t)}{R(t)} \tag{2}$$

In practical applications, $\eta_d$ and $\eta$ will be calculated for discrete time steps $[t_n, t_n+\Delta t]$. For a discrete time step, these quantities are redefined as:

$$\eta_d(d,t_n) = \frac{\int_{t_n}^{t_n+\Delta t} R^*(d,t)\,dt}{\int_{t_n}^{t_n+\Delta t} R(d,t)\,dt} = \frac{S^*(d,t_n)}{S(d,t_n)} \quad (3)$$

$$\eta(t_n) = \frac{\int_{t_n}^{t_n+\Delta t} R^*(t)\,dt}{\int_{t_n}^{t_n+\Delta t} R(t)\,dt} = \frac{S^*(t_n)}{S(t_n)} \quad (4)$$

where $S^*(d,t_n)$ and $S(d,t_n)$ are the hydrological rainfall sum and the reference rainfall sum for raindrops of diameter d during the time step (accumulated rainfall over the time step). $S^*(t_n)$ and $S(t_n)$ refer to the same quantities but integrated over the entire spectrum of raindrop diameters. When $\eta$ has been determined, the corresponding hydrological rainfall sum can be calculated by multiplying the catch ratio by the reference rainfall sum.

The influencing parameters of the catch ratio $\eta$ are the six quantities listed above. If we limit the study to two dimensions (eliminating wind direction as a variable), if we focus on a given topography and on a given position on the topography, and if we assume a raindrop-size distribution that provides a unique relationship between the raindrop spectrum and the reference rainfall intensity, then $\eta$ is unambiguously defined by two variables: reference wind speed and reference rainfall intensity.

*Numerical model*

Full numerical modelling of the WDR effect consists of five main steps:

(1) The calculation of the steady-state wind-flow pattern over the topography with a Computational Fluid Dynamics (CFD) code. It comprises the construction of a model of the topography in a computational domain and the discretisation of the domain by dividing it into a large number of control volumes (i.e. computational cells). Important boundary conditions are the wind-speed inlet profile and the surface roughness. The type and values of these boundary conditions will be explicitly mentioned in this paper for every numerical simulation. Because they are not specific features of the numerical WDR model but of all numerical models for wind-flow simulation in the atmospheric boundary layer, general information about these boundary conditions has been provided in Appendix A. Based on the boundary conditions, the complex 3D or 2D Reynolds-Averaged Navier-Stokes (RANS) equations in combination with the equations of the selected turbulence model are solved for each of the cells in the computational domain. The results of the CFD calculations are the numerical values of wind speed (x,y,z-component), pressure and turbulence quantities at the centre of each cell.

(2) In the calculated wind-flow field, raindrop trajectories for raindrops of different sizes are determined by solving the raindrop's equation of motion.

(3) The specific catch ratio $\eta_d$ is subsequently determined based on the configuration of the raindrop trajectories using the following procedure. Figure 2 illustrates the situation in two dimensions. In a steady-state wind-flow pattern, two raindrop trajectories of diameter d form a stream tube. Let $\overrightarrow{R_d}$ represent the rainfall-intensity vector related to raindrops of diameter d (L/m²h). The flux of this vector through the horizontal surface $A_h$ that is situated outside the disturbed wind field is equal to the product of the reference rainfall intensity R(d) (L/m²h) and the surface area $A_h$. This volume of rainfall per hour (L/h) flows through the stream tube and falls on the slope surface $A_s$. Conservation of mass for the raindrops in the stream tube allows the catch ratio $\eta_d$ to be expressed in terms of areas:

$$\eta_d(d) = \frac{R^*(d)}{R(d)} = \frac{A_h}{A_s\cos\theta} \quad (5)$$

Here, $A_s\cos\theta$ is the horizontal projection of the slope area $A_s$ that is bounded by the trajectory endpoints. In the simulation, it is important that the injection positions of the raindrops (and hence the location of the plane $A_h$) are situated sufficiently high and far upstream to allow the raindrops to reach their terminal velocity of fall (vertical) and the wind velocity (horizontal) before entering the flow pattern disturbed by the topographic feature.

(4) The catch ratio $\eta$ for a given reference rainfall intensity is obtained by integrating the specific catch ratio $\eta_d$ over the appropriate raindrop-size distribution.
(5) When the former four steps are executed for a number of reference wind-speed values and reference rainfall intensities, charts are obtained containing $\eta$ as a function of these two parameters. Based on this knowledge, the hydrological rainfall sum can be obtained in time and space for any meteorological data record following the model developed in (Blocken *et al.*, 2004).

The accuracy of the numerical results is to a large extent determined by four important modelling choices: the turbulence model, the computational mesh, the raindrop drag coefficients and the raindrop-size distribution.

(1) The turbulence model that is selected for the present study is the "realizable" k-ε model developed by Shih *et al.* (1995). It is used in combination with non-equilibrium wall functions (Kim and Choudhury, 1995). This combination has been shown to exhibit superior performance for flows with adverse pressure gradients, separation and recirculation (Shih *et al.*, 1995), (Kim *et al.*, 1997), (Kim and Choudhury, 1995). These flow features are often encountered in the flow over topographical configurations such as hills, cliffs, ridges and valleys. Furthermore, the use of these models has been proven to provide accurate quantitative predictions of the WDR distribution on the vertical faces of obstacles (buildings) (Blocken and Carmeliet, 2000; 2002).
(2) The adequacy of the computational mesh (discretisation) on which the RANS equations and turbulence model equations are solved is checked by estimating the numerical discretisation error by comparing meshes with increasing refinement as explained in (Blocken *et al.*, 2004).
(3) In the raindrop trajectory calculations, appropriate measured raindrop drag coefficients published by Gunn and Kinzer (1949) are used. These values take into account the non-spherical form of falling raindrops, as opposed to the often-used drag coefficients of Morsi and Alexander (1972).
(4) The raindrop-size distribution f(d) is generally not measured. An empirical raindrop-size distribution is used in the model. The formula of Best (1950) has been adopted because of the extent of the study carried out by this author. For use in the present model, the raindrop-size distribution by Best (applying to the size distribution in a volume of air) has to be converted to the raindrop-size distribution as a flux through a horizontal plane. The reason is that due to the variation of the terminal velocity of fall of a raindrop with size, the raindrop-size distribution in the air differs from the raindrop-size distribution through a horizontal plane. The former can be converted to the latter by multiplying with the raindrop terminal velocity of fall:

$$f_h(d) = \frac{f(d)\, v_t(d)}{\int_d f(d)\, v_t(d)\, d\,d} \tag{6}$$

where $f_h(d)$ represents the raindrop-size distribution through a horizontal plane, f(d) the raindrop-size distribution in the air and $v_t(d)$ the terminal velocity of fall of a raindrop with diameter d. The denominator is necessary to ensure that the area under the curve "$f_h(d)$ versus d" remains equal to unity. Results of raindrop terminal velocity measurements can be found in e.g. Gunn and Kinzer (1949). The size distribution $f_h(d)$ is presented in Figure 3 for various reference rainfall intensities. Note that the raindrop-size distribution by Best provides the requested unique relationship between the raindrop spectrum and the reference rainfall intensity.

## APPLICATION AND EXPERIMENTAL VERIFICATION

A review of the literature points out that very little experimental information has been published in a form suitable for experimental verification of the CFD model. In many cases, the reference wind speed, reference wind direction and/or reference rainfall intensity during the measurements are not provided and/or sometimes it is not even indicated whether the rain measurements were made with horizontal or tilted orifice gauges. In other cases, the measurements showed too much scatter for a fixed WDR distribution profile over the topography to be discerned.

Four studies that provide measurements/observations fit for purpose are selected for use in this study:

(1) Sandsborg (1970): hydrological rainfall measurements on a small isolated hill;
(2) Craig (1980): observations of wind speed and drift of drizzle over a succession of two cliffs;

(3) Sharon *et al.* (1988): hydrological rainfall measurements in a cotton field with ridges and furrows;
(4) Sharon and Arazi (1997): hydrological rainfall measurements in a small valley.

The WDR distribution over each of these configurations is modelled and compared with the corresponding measurements. The results are presented below. They can be ordered in several ways: according to the size of the topography, the shape of the topography, or according to the quality of the experimental data for verification purposes. The latter option is selected. The effort of numerical modelling (i.e. the number of steps in the numerical model that are executed) is increased with increasing suitability of the experimental data. It is noted that the fifth step of the numerical model will not be executed in the present paper, as no detailed temporal experimental data records were available.

*Succession of two steep cliffs (Craig, 1980)*

Geometry and observations

The study area is situated in east County Antrim, Northern Ireland. It is characterised by steep, irregular slopes with two major cliffs. The geometry is illustrated in Figure 4. The two cliffs are respectively about 30 and 20 m high and stand at approximately 85° from the horizontal. The amount of rainfall data provided is limited, but some interesting remarks were made by the author. He suggested that vortices were formed in the lee of the cliff faces, as indicated in Figure 4. He stated that this would explain the fact that higher precipitation amounts were observed at some distance from the cliff than just beyond it (especially for snow and drizzle), (see Figure 4) and the fact that the surface near the cliff bases was frequently in calm air while some 100 m downslope the wind was strong and gusty. The numerical modelling effort will concentrate on the reproduction of these features.

Numerical modelling and experimental verification

The geometry of the area, according to the information provided in the publication (Craig, 1980, p. 302, Figure 1) is wide and could be represented by 2-dimensional modelling. The transect as provided by the author (and also displayed in Figure 4) is modelled. Part of the computational mesh is shown in Figure 5a. The size of the cells increases from bottom to top of the domain, from 3 m near the surface to 120 m at the top. The choice of the mesh size is based on the restriction that the discretisation error (defined here as the difference between the solution obtained on the current mesh and the solution obtained on a very fine reference mesh – with cells that are 16 times smaller) should be no larger than 5%. More details about this procedure are outlined in (Blocken *et al.*, 2004) and will in the interest of brevity not be duplicated here. Wind-flow is calculated for reference wind-speed values $U_{10}$ = 10 and 20 m/s, where the reference height h is taken 10 m above the 200 m plateau. The vertical inlet wind-speed profile takes into account the fact that the wind speed increases with height. In this paper, it is represented by a power-law function with exponent $\alpha_P$ = 0.15 (Davenport, 1960; 1961). The surface roughness $K_S$ is taken 0.1 m. (More information about these boundary conditions is provided in Appendix A). Figure 5b illustrates calculated wind-velocity vectors, where the length of each vector is a relative measure for its magnitude at that location. As suggested by Craig, two vortices are identified, but they are situated further downstream and the second vortex is much larger than suggested. It is observed that the surface beyond the first cliff is clearly sheltered from wind, while further downstream, higher wind-speed values are found at ground-level. This corroborates the statements by Craig (1980). Beyond the second cliff however, high ground-level wind speed is found almost everywhere. This is illustrated by zooming into Figure 5b. Figure 5c and 5d display trajectories of 0.3 mm diameter raindrops (representing drizzle) that have been injected in the $U_{10}$ = 10 m/s and 20 m/s flow field. They have been released equidistantly from a straight horizontal line at a height of about 300 m (100 m above the top of the topography). It is observed that the rain is driven nearly horizontally over the edge and, when entering the region of the vortices, is suddenly directed towards the ground surface. For $U_{10}$ = 10 m/s, the uneven distribution of raindrops is not so clear, but for 20 m/s, clearly a higher concentration of raindrops (reduced spacing between trajectories) is observed away from the cliffs, almost on the same locations as reported by Craig (Figure 4). In conclusion, the existence of zones of low wind speed just beyond the cliffs and of zones of high wind speed at a certain distance downstream of the cliff faces can be reproduced for the first cliff, but not for the second. The numerical results confirm Craig's suggestion that the vortices are responsible for the redistribution of rainfall and correspond with Craig's statement about low and high rainfall areas.

*Small isolated hill (Sandsborg, 1970)*

Geometry and measurements

The study area is located somewhere in Sweden. Hydrological rainfall measurements were conducted on the sides and the crest of a hillock, a few meters in height and some tens of meters in length. The surroundings of the hillock consisted of flat, cultivated country up to a distance of 200 m. The hill itself was covered with very short grass. Measurement data is presented by means of precipitation maps with isohyets. During one of the presented rain periods, the wind direction was steady from SSW, and the mean wind speed during the period was given (4.6 m/s at a height of 9 m). This made it possible to numerically simulate this situation. However, neither the reference rainfall intensity nor the rainfall duration was indicated in the paper and these values could also not be estimated from other data in the text. An estimate for the total reference rainfall sum S is obtained by averaging the volume of hydrological rainfall measured by all the gauges on the hill. To prepare the data for the simulation, we made a transect cutting in SSW direction through the hill and we determined the measurement values along the transect from the precipitation map in the paper. The geometry of the transect, together with the transformed measurements (catch ratio $\eta$, i.e. S* reported by Sandsborg divided by the estimate for S) is indicated in Figure 6a and b. The wetting pattern clearly shows an excess of rain on the windward slope near the crest and a deficit of rain on the leeward slope just beyond the crest. This observation is opposite to observations of other authors (James, 1964), (Hovind, 1965), which has caused some confusion in the literature (Reid, 1973), but it can be explained by the fact that the measurements of the latter authors were meteorological rain measurements on hills (Figure 1b), whereas those of Sandsborg are hydrological ones (Figure 1c).

Numerical modelling and experimental verification

The hill is a 3D feature although its upper part is somewhat stretched from SE to NW (i.e. approximately perpendicular to the SSW wind direction) (Sandsborg, 1970, p. 239, Figure 3). This situation will be approximated by 2D modelling. The wind-flow over and the distribution of WDR on the transect are modelled. The mesh size near the surface of the hillock is taken 0.15 m and it increases with height to a value of 3 m at the top of the computational domain (Figure 7a). A power-law wind-speed profile with exponent $\alpha_P = 0.15$ is used as inlet into the domain. The roughness $K_S$ of the hillock itself is taken 0.03 m (very short grass). The wind-flow field is illustrated in Figure 7b. It shows high wind speed over the windward slope and over the crest of the hill, and a large recirculation vortex with low wind-speed values on the lee side. Raindrop trajectories are displayed in Figure 7c and d. The trajectories of the small drops are significantly influenced by the wind-flow pattern. The curvature towards the vertical of the trajectories in the lee of the hill is caused by the recirculation vortex and the low wind speed in that vortex. For a number of raindrop sizes, the specific catch ratio $\eta_d$ is determined (Figure 6c). The modelling effort is not taken further than the determination of $\eta_d$ because no information about reference rainfall intensity during the spell is available. To verify the simulation, the values of $\eta_d$ for individual drops (Figure 6c) are compared with the measured values (Figure 6b). Taking into account the limitations of 2D modelling of the 3D hill and the fact that we obtained the measured WDR profile from a precipitation map with only a few isohyets, a fair agreement is obtained. Both the excess of WDR in front of the crest and the deficit beyond it are predicted. The location of the latter is well predicted, but the location of the former is in reality situated a few meters more upstream. Figure 8 illustrates the correspondence/discrepancies between the numerical and the experimental results. The numerical model somewhat underestimates the lower and overestimates the higher $\eta$-values.

*Small valley (Sharon and Arazi, 1997)*

Geometry and measurements

The small valley, Lehavim-N, is a watershed situated 12 km to the north of Beersheba, in Israel. The region is characterised by local relative heights of about 50 m with slope gradients between 15 and 25°. The surface is sparsely covered by a very low shrub vegetation. Wind direction during rain is generally from SW to W. The geometry of a W-E transect of the valley is illustrated in Figure 9a. An extensive and detailed rain-gauge measuring network was established at Lehavim-N. Among others, it included ten measuring positions along an approximately W-E oriented transect, as indicated in Figure 9a. At each position, hydrological and meteorological rainfall measurements were made. Wind speed was measured at a local hill top situated about 500 m south of the transect. The measurements reported in this paper were specifically intended to provide an empirical basis to verify numerical models. As a consequence,

the authors have organised their measurement data in tables and have conscientiously analysed the results. The measurements revealed a reversed surface flow in the lower part of the valley, indicating the existence of a vortex that significantly influenced the rainfall distribution. The hydrological measurements S* by Sharon and Arazi are displayed in Figure 9b. They have been converted to $\eta$-values by dividing S* by an estimate of S. The latter is obtained by averaging the hydrological rainfall measured at all 10 stations along the transect. For each wind-speed class, a distinct and similar wetting pattern is present. Peak values are found at station 4 and 7, while lower rain amounts are present at station 6 and 9. Numerical modelling will be used in an attempt to predict the existence and the extent of the vortex in the valley and to determine the WDR distribution along the W-E transect.

Numerical modelling and experimental verification

The valley is a definite 3D feature. Nevertheless 2D modelling will be performed, but only with the intention to predict the main features in a qualitative way. The transect shown in Figure 9a is modelled. The mesh size increases from 1 m near the surface to 10 m at the top of the domain (Figure 10a). The power-law wind-speed inflow profile has an exponent $\alpha_P = 0.20$ and the surface roughness $K_S$ is taken 0.10 m (sparse and very low shrub vegetation). Figure 10b-d illustrate the wind field and some raindrop trajectories. The vortex identified by Sharon and Arazi (1997) is clearly predicted. Its height is about half the depth of the valley. Along the lower half of the windward slope, the flow at the surface is reversed, while it goes upward along the upper half of the slope. This is in direct agreement with the measurements reported by Sharon and Arazi (Sharon and Arazi, 1997, p. 37, Figure 10). The raindrop trajectories that enter the vortex are curved towards the valley surface. The other trajectories move over the vortex, maintain their inclination and impact on the upper part of the windward slope. In modelling the conditions presented in the paper by Sharon and Arazi (1997), it is assumed that the measured wind speed is approximately the same as the one that would occur at 10 m upstream and above the downstream valley edge in the 2D model ($U_{10}$). This assumption could not be verified: a complex 3D CFD model of the entire valley and its surroundings would be needed to determine the ratio between both wind-speed values. This is considered not necessary for the present qualitative verification study: as shown in Figure 9b, an over- or underestimation of the wind speed will only affect the profile in an absolute and not in a relative way. No information about rain intensity was provided in the paper by Sharon and Arazi (1997). Therefore, only $\eta_d$ is calculated for a few drop diameters (Figure 11a-c). Comparing the calculated profiles with the corresponding measurement results, the following observations are made: (1) the profiles for the small to medium drop sizes (0.8 and 1 mm) show the best correspondence with the measurements. (2) For these drop sizes, the first dip at position 9 is predicted, but the peak at position 7 is predicted to be situated at position 8. (3) The dip at position 6 is generally predicted but not as pronounced as in reality. (4) The increase from position 6 towards the peak at position 4 and the subsequent decrease towards position 1 are well predicted. (5) Taking into account the limitations of 2D modelling of the 3D valley, a satisfactory qualitative agreement is obtained.

*Small ridges and furrows in a cotton field (Sharon et al., 1988)*

Geometry and measurements

The study site is part of the cotton fields of Kibbutz Alumim in the flatlands of the Southern Coastal Plain of Israel. It consists of two experimental plots, each containing a series of parallel ridges. In one of the plots the ridges are oriented NE-SW, while in the other their orientation is SE-NW. The ridges are 0.3 to 0.4 m high with a distance in between of about 1.1 to 1.2 m. Figure 12 shows a cross-section (transect) of two ridges. The measurements and measurement conditions were well documented. Hydrological rainfall measurements were made for four transects in the field, two with NE-SW orientation (50°-230°) and two with SE-NW orientation (145°-325°). Each transect consisted of two slopes and a furrow bottom (as in Figure 12). Measurements were taken at 7 locations along the transect (Figure 12), yielding 28 measuring points in total. No significant differences were found between the three measurements on the same slope. The same went for the differences between each set of two identically oriented slopes. Therefore, Sharon *et al.* (1988) averaged these values, yielding a single value for each slope with a different orientation (NE, SW, SE, NW). Measurement results were reported for a number of rainstorms. The general data for the storms that were made available by Sharon *et al.* (1988) and that will be used for the experimental verification in this paper are given in Table 1. The reference rainfall sum (S) mentioned here was obtained as the average of all 28 hydrological rainfall measurements. Wind conditions during rainfall were measured with autographic recorders at 1.2 and 3.5 m above the ground. In Table 1, each storm is split up into several parts, each with approximately uniform wind conditions and with a given percentage

of total rainfall. Sharon *et al.* (1988) noted that the residual percentage of rainfall (that is not specified in Table 1 and for which no further information was made available) occurred with variable wind from other directions. As an example, hydrological rain measurements taken after storm 9 are given in Table 2. The SW and NW oriented slopes clearly receive most rain, because wind direction during the storm was WSW.

Numerical modelling and experimental verification

The large length of the ridge rows compared to the ridge height (length is about 16 to 18 m, (Sharon *et al.*, 1988), p. 1717, Figure 3a) justifies a 2D modelling approach (Moss and Baker, 1980, referring to guidelines for obstacles of simple geometry set forth by Brederode and Bradshaw, 1972). A model representing a succession of six ridges is constructed. This allows us to investigate the difference in WDR distribution for ridges at the edge and for ridges in the middle of the field. The size of the computational mesh is increased from 0.04 m near the ground surface to 0.3 m at the top of the domain (Figure 13a). A power-law wind-speed profile with exponent $\alpha_P = 0.15$ corresponding to the roughness of flat cultivated terrain is used. The roughness of the surface of the ridges, $K_S$, is taken 0.01 m. Wind-flow over the first three ridges is illustrated in Figure 13b. The windward slope of the first ridge (at the edge of the field) is clearly subjected to different wind conditions compared to the other ridges. Flow separation occurs at the top of the ridges causing recirculation vortices in each of the cavities (furrows). Trajectories of 1.0 mm raindrops in the $U_1 = 4$ m/s and 8 m/s wind-flow field are given in Figure 13c and d. The wetting pattern is almost the same for the ridge at the edge and the other ridges. Another important observation is that, above a certain wind speed, the leeward slope and the furrow bottom are sheltered from rain (Figure 13d). These observations are also evident from the profiles of $\eta_d$ (Figure 13e-f, where the dashed lines at the bottom of the figure indicate the position of the six ridges). It is clear that for even higher wind-speed values, also the windward slopes of all ridges but the first will become partly sheltered. Integrating $\eta_d$ over the raindrop spectrum, profiles for the catch ratio $\eta$ are obtained for different reference rain intensities (Figure 13g-h).

This procedure is used to calculate the WDR sum falling on the ridge slopes and bottoms for each of the storms given in Table 1 (note that one of the storms mentioned in the paper by Sharon *et al.* is not considered for this study, as no information on rainfall intensity was available for this storm). The complete procedure is executed for both transects (NE-SW and SE-NW) and for each part of the rainstorm. The calculation is summarized in Appendix B, Table B.1, for the case of storm 9. The wind vector (wind speed and direction) is projected parallel to each of the transects. Simulations of the wind-flow are then made with the projected wind-speed values. Raindrop trajectories are calculated for raindrops from 0.5 to 1 mm in steps of 0.1 mm, from 1 to 2 mm in steps of 0.2 mm and from 2 to 6 mm in steps of 1 mm. For each of the raindrop sizes, $\eta_d$ is obtained. The value of $\eta$ results from integrating $\eta_d$ using the raindrop-size distribution corresponding to the reference rain intensity for the given storm part. It is noted that $\eta$ for the residual part of each storm (for which no measurement data is available, see Table 1) is assumed to be equal to unity at all positions, which means that we assume a net zero wind speed over this time period. An equal assumption was also made by Sharon *et al.* (1988). Finally, the hydrological rainfall sum S* for each storm part is obtained by multiplying $\eta$ with the corresponding reference rainfall sum. Table 3 compares the calculated and measured S* for all storms. A good agreement is obtained for each storm. The correspondence between the numerical and the experimental results is indicated graphically in Figure 14.

## DISCUSSION

An important assumption in the present paper is the use of 2D numerical modelling to determine the WDR distribution on essentially 3D topographic configurations. As mentioned before, this assumption is valid if the width of the topography is large compared to its other dimensions. This was more or less the case for the succession of cliffs and certainly the case for the field with ridges and furrows. 2D modelling is probably the main cause for the discrepancies between the numerical and the experimental results for the case of the small isolated hill and the small valley. Especially for the latter, 3D reality can differ from the 2D situation. This is clearly indicated by Sharon and Arazi (1997) who identified the 3D behaviour of the wind-flow pattern in the valley based on their measurements. Therefore, the verification study conducted for this case should in the first place be regarded as a qualitative verification. Taking into

account this remark, a good agreement with the experiments has been obtained for all the cases that were studied.

Comparing the raindrop trajectories in the flow field over the ridges and furrows (Figure 13c-d) with the trajectories calculated in the other cases (Figures 5c-d, 7c-d, 10c-d), it is observed that the former are only very weakly influenced by the disturbed wind-flow field. As a result, the trajectories are almost rectilinear. The wind-flow pattern that is disturbed by the ridges appears to be too small to significantly influence the raindrop trajectories. This is the reason why the value of $\eta$ on the ridges at the edge of the field is not very different from that on ridges in the middle, although the wind-flow pattern at these locations is very different. It also confirms the decision of Sharon *et al.* (1988) to average the hydrological rainfall sums measured on identically oriented slopes that were situated on different locations in the field.

In their research paper on ridges and furrows, Sharon *et al.* (1988) applied a trigonometric model to predict the WDR sum along the transects. This model is based on the cosine law from spherical geometry and should apply to any point in the field (Fourcade, 1942), (Sharon, 1980): Eq. (7).

$$S^* = S\left(1 + \mathrm{tg}\alpha\ \mathrm{tg}\beta\ \cos(z\alpha - z\beta)\right) \tag{7}$$

where S* and S are the hydrological rainfall and the reference rainfall at the point, respectively, $\alpha$ is the local inclination of the ground surface at that point relative to the horizontal, $\beta$ is the inclination of the rainfall relative to the vertical, $z\alpha$ is the aspect of the ground surface at that point and $z\beta$ is the direction from which the rain is coming. These variables and an example calculation with this formula for three points on the ridges' geometry are illustrated in Figure 15. This formula assumes that the raindrop trajectories are straight lines. Using this model to predict the WDR distribution on the ridges, Sharon *et al.* (1988) found a remarkably good agreement. They attributed this to the small topographical scale. This is confirmed by Figure 13c-d: the raindrop trajectories are indeed almost straight lines. In cases such as these, the trigonometric model is a valuable tool. Furthermore, the trigonometric model is much simpler and easier to apply than the full numerical modelling procedure performed in this paper. However, the trigonometric model has a number of important drawbacks compared to the numerical model:

1. For a given topography, it is generally not known in advance whether the raindrop trajectories are rectilinear or not and hence whether the trigonometric model is applicable or not. Its use is justified when the disturbance of the wind-flow pattern by the topography can be bridged by the raindrop without influence on its course. This is the case for large raindrops and/or small disturbances (small topographical scale). Poreh and Mechrez (1984) and Sharon *et al.* (1988) have addressed the importance of the topographical scale on the WDR distribution. However, guidelines indicating, as a function of topography and raindrop diameter (or rainfall intensity) whether the raindrop trajectories can be considered rectilinear or not, have yet to be defined.
2. Even if the raindrop trajectories can be considered rectilinear, an important deficiency of the trigonometric model is that it is unable to take into account the shelter effect that part of the topography can have over other parts. Focusing on the ridges, Figure 13d illustrates that the bottom between the ridges is sheltered by the ridge in front of it. This means that the rainfall reaching this part is zero. Eq. (7) however, for a point on the horizontal surface ($\alpha = 0$), gives S* = S. At higher wind speeds, this error will also contaminate the results on the windward slope (as also this will be partly sheltered from rain). It is noted that for the storm data given in Table 1, practically all wind-speed values (projected) were too small for this error to have effect. High wind speeds were observed only during storm 9, (14 m/s), but only very little rain fell during this period. For higher wind-speed values and/or rainfall sums and for other topographical configurations, the use of the trigonometric model – without appropriate adjustments for the shelter effect – can give rise to large errors.

## CONCLUSIONS

- The wind-driven-rain distribution over four different topographic configurations has been numerically modelled and the numerical results have been compared with experimental data. The study included a succession of cliffs, a small isolated hill, a small valley and a field with ridges and furrows. For all four cases, a fair to good agreement has been found. It has been shown that the numerical model can predict (1) the existence of the specific wind-flow pattern (including vortices) associated with topographic features, (2) the influence of the wind-flow pattern in general and of vortices in particular

on the raindrop trajectories, (3) the specific distribution patterns of wind-driven-rain over micro-scale topography.

- Some discrepancies between the numerical and the experimental results have been observed, especially for the case of the small isolated hill and the small valley. It is believed that the main reason for these discrepancies is the use of 2D modelling for these essentially 3D features. Nevertheless, even in these cases, the 2D model has proven its capability to predict the main features of the wind-flow pattern and the wind-driven-rain distribution, at least qualitatively.
- The simpler trigonometric model (Fourcade, 1942), (Sharon *et al.*, 1988) can provide an alternative for full numerical modelling, but only on the strict condition that the topographical scale is small enough for the raindrop trajectories to be rectilinear. It is difficult however to predict when this condition will be satisfied. It is believed that full numerical modelling is a useful tool to determine the topographical boundaries below which the trigonometric formula can be applied. But even then, this simplified formula has to be used with care because it does not take into account the shelter effect that part of the topography can exert on other parts. The shelter effect can easily be taken into account by constructing additional formulae that however will be different for different geometric configurations. Full numerical modelling is more complex but also far more widely applicable. Sharon *et al.* (1988) adequately illustrated that the trigonometric formula could well be applied for the case of the field with ridges and furrows. But it is clear that it cannot be used for the three other case studies treated in this paper because of the large influence of the wind field on the raindrop trajectories.
- The full numerical model is a valuable tool to determine the wind-driven-rainfall distribution over any type of micro-scale topography. Apart from that, it is believed that the different steps that constitute the model (calculation of wind-flow field, raindrop trajectories, specific catch ratio, catch ratio) provide important insights into the interaction between wind, rain and micro-scale topography.
- Finally, we would like to stress that the present modelling and verification study is only a first step. It has been performed with 2D modelling and has been based on the experimental data that is currently available in the literature. Additional verification and validation efforts would greatly benefit from (1) the availability of suitable experimental data for a wide range of other topographical configurations and (2) from the availability of detailed spatial and temporal (e.g. 10-minute or hourly) wind, rain and wind-driven-rain measurements that would allow a verification of the simulation of the wind-driven-rain distribution in space and time. The application and verification of the numerical model in this paper has yielded promising results. Together with the use of new and additional experimental data, the use of 3D modelling should provide further information on the capabilities and performance of full numerical modelling.

## ACKNOWLEDGEMENTS

The authors want to express their gratitude to the researchers that have published their experimental data in a form suitable for the experimental verification conducted in this paper.

This research is funded by the government of Flanders. The first author has held a Ph.D. scholarship of the IWT-Flanders and is currently a post-doctoral research engineer of the FWO-Flanders. The IWT-Flanders (Institute for the Promotion of Innovation by Science and Technology) supports and stimulates research and technology transfer in the Flemish Industry. The FWO-Flanders (Fund for Scientific Research) supports and stimulates fundamental research in Flanders. Their contribution is gratefully acknowledged.

## APPENDIX A

Information on two boundary conditions, being the wind-speed profile and the surface roughness for the CFD simulations, is provided. The vertical wind-speed profile of the wind flow over a terrain with uniform roughness can be represented by the logarithmic law or by the power law. The logarithmic law is first explained. It is given by Eq. (A.1):

$$U(y) = \frac{u^*}{\kappa} \ln\left(\frac{y + y_0}{y_0}\right) \tag{A.1}$$

where U(y) is the mean wind speed at height y, u* is the friction velocity, $\kappa$ is the Von Karman constant ($\approx 0.42$) and $y_0$ is the aerodynamic roughness length. The friction velocity is a variable that represents the magnitude of the velocity fluctuations in the turbulent boundary layer. The aerodynamic roughness length $y_0$ depends on the nature of the roughness elements on the surface: size, shape, orientation and spacing. It is not a real height; rather it should be regarded as an "equivalent roughness that is felt by the flow". Panofsky and Dutton (1984) mention that it can be interpreted as a measure of the size of the eddies at the surface. For wind engineering purposes, a roughness classification has been developed by Davenport and it has been updated by Wieringa (1992). It is given in Table A.1. Given the description of the terrain, its aerodynamic roughness length $y_0$ can be determined from this classification. It is important to note that extracting a roughness length from Table A.1 is only allowed if the landscape description used as input for the table is estimated based on an upstream length (fetch) of at least 5 km.

Instead of the logarithmic law, the power law can be used. It is given by Eq. (A.2):

$$\frac{U(y)}{U_{ref}} = \left(\frac{y}{y_{ref}}\right)^{\alpha_P} \tag{A.2}$$

where $U_{ref}$ is a reference mean wind speed at height $y_{ref}$ and $\alpha_P$ is the power-law exponent, which expresses the roughness of the terrain (fetch at least 5 km). The aerodynamic roughness length $y_0$ and the power-law exponent $\alpha_P$ are related. The relation can be found by matching both laws. The two laws cannot be matched exactly, but matching can be performed at a certain (chosen) height, e.g. the reference height. Fig. B.1 illustrates the logarithmic law (with $y_0 = 0.03$ m) and the power law (with $\alpha_P = 0.17$), both with a wind speed U = 10 m/s at a matching height y = 10 m. Note that either of both laws could be used in the present paper, but that the power law was chosen because it is more frequently used in engineering applications.

The logarithmic law or the power law are used to describe the wind-speed profile that enters the computational domain (inlet boundary condition). They take into account the effect of the roughness of the "distant" terrain (i.e. the terrain that is not included in the computational domain) on the wind-speed profile. The surface roughness, $K_S$, on the other hand, describes the local roughness at the bottom of the computational domain (ground boundary condition). It is an equivalent sand-grain roughness that is generally different from $y_0$. More information can be found in e.g. Durbin and Petterson Reif (2001).

## APPENDIX B

A brief explanation is given of the procedure used to calculate the hydrological rainfall sum S* on the ridges and furrows of the cultivated field. Table B.1-a contains the storm data for storm 9, including reference meteorological rainfall sum S, intensity R, reference wind speed and wind direction. Table B.1-b and B.1-c each contain the calculation for one of the two transects. First, the wind-velocity vector (i.e. wind speed and wind direction) mentioned in Table B.1-a is projected along the transect and the resulting wind-speed component ($U_1$) is given in both tables. Next, for this value of reference wind speed and for the reference rainfall intensity R given in Table B.1-a, the catch ratio $\eta$ at both slopes and at the bottom is extracted from the numerical simulation data (e.g. Figure 13g and h). The hydrological rainfall sum S* for each storm part is determined by multiplying the $\eta$-values with the corresponding reference rainfall sum S in the storm part (Table B.1-a, third column). Finally, at the bottom of Table B.1-b and B.1-c, the sum of S* over all storm parts is made and the resulting values are compared with the measurements.

## REFERENCES


Arazi A, Sharon D, Khain A, Huss A, Mahrer Y. 1997. The windfield and rainfall distribution induced within a small valley: field observations and 2-D numerical modelling. *Boundary-Layer Meteorology* **83**: 349-374.

Best A.C. 1950. The size distribution of raindrops. *Quarterly Journal of the Royal Meteorological Society* **76**: 16-36.

Blocken B, Carmeliet J. 2000. Driving rain on building envelopes – I: numerical estimation and full-scale experimental verification. *Journal of Thermal Envelope and Building Science* **24**(1): 61-85.

Blocken B, Carmeliet J. 2002. Spatial and temporal distribution of driving rain on a low-rise building. *Wind and Structures* **5**(5): 441-462.

Blocken B, Carmeliet J, Poesen J. 2004. Numerical simulation of the wind-driven rain distribution over small-scale topography in space and time. *Journal of Hydrology*, accepted for publication. 2004.
Bradley SG, Gray WR, Pigott LD, Seed AW, Stow CD, Austin G.L. 1997. Rainfall redistribution over low hills due to flow perturbation. *Journal of Hydrology* **202**(1-4): 33-47.
Brederode V, Bradshaw P. 1972. Three-dimensional flow in nominally two-dimension separation bubbles. I. Flow behind a rearward-facing step. *Imp. College Aero. Rep*: 72-19.
Choi ECC. 2002. Modelling of wind-driven rain and its soil detachment effect on hill slopes. *Journal of Wind Engineering and Industrial Aerodynamics* **90**(9): 1081-1097.
Craig D. 1980. Two examples of the effect of topography on rainfall distribution patterns. *Weather* **35**(10): 301-307.
Davenport AG. 1960. Rationale for determining design wind velocities. *Journal of the Structural Division, Proceedings American Society Civil Engineers* **86**: 39-68.
Davenport AG. 1961. The application of statistical concepts to the wind loading of structures. *Proceedings Institution of Civil Engineers*, August.
De Lima JLMP, Van Dijk PM, Spaan WP. 1992. Splash-saltation transport under wind-driven rain. *Soil Technology* **5**: 151-166.
De Lima JLMP. 1989. Raindrop splash anisotropy : slope, wind and overland flow velocity effects. *Soil Technology* **2**: 71-78.
De Lima JLMP. 1990. The effect of oblique rain on inclined surfaces: a nomograph for the rain-gauge correction factor. *Journal of Hydrology* **115**: 407-412.
Disrud LA, Krauss RK. 1971. Examining the process of soil detachment from clods exposed to wind-driven simulated rainfall. *Transactions of the ASAE* **14**: 90-92.
Disrud LA. 1970. Magnitude, probability, and effect on kinetic energy of winds associated with rain in Kansas. *Transactions Kans. Acad. Sci.* **73**(2): 237-246.
Durbin PA, Petterson Reif BA. 2001. *Statistical Theory and Modeling for Turbulent Flows*. John Wiley & Sons, Chichester.
Erpul G. 2001. *Detachment and sediment transport from interrill areas under wind-driven rain*. Unpublished PhD thesis, Purdue University; 171.
Erpul G, Norton LD, Gabriëls D. 2002. Raindrop-induced and wind-driven soil particle transport. *Catena* **47**(3): 227-243.
Erpul G, Norton LD, Gabriëls D. 2003a. The effect of wind on raindrop impact and rainsplash detachment. *Transactions of the ASAE* **46**(1): 51-62.
Erpul G, Norton LD, Gabriëls D. 2003b. Sediment transport from interril areas under wind-driven rain. *Journal of Hydrology* **276**(1-4): 184-197.
Fourcade HG. 1942. Some notes on the effects of the incidence of rain on the distribution of rainfall over the surface of unlevel ground. *Transactions of the Royal Society of South Africa* **29**(3): 235-254.
Gabriels D, Tack K, Erpul G, Cornelis WM, Norton LD, Biesemans J. 1997. Effect of wind-driven rain on splash detachment and transport of a silt loam soil: a short slope wind tunnel experiment. In: *Proceedings of Workshop on Wind and Water Erosion*, November 17-18 1997, Ghent, Belgium; 87-93.
Geiger R. 1965. *The climate near the ground*. Harvard University Press: Cambridge; 611.
Goossens D, Poesen J, Gross J, Spaan W. 2000. Splash drift on light sandy soils: a field experiment. *Agronomie* **20**: 271-282.
Gunn R, Kinzer GD. 1949. The terminal velocity of fall for water droplets in stagnant air. *Journal of Meteorology* **6**: 243-248.
Hamilton EL. 1954. Rainfall sampling on rugged terrain. *Tech. Bull. U.S. Dep. Agric.*, No. 1096, 41p.
Hayes GL, Kittredge J. 1949. Comparative rain measurements and raingage performances on a steep slope adjacent to a pine stand. *Transactions AGU* **30**(2): 295-301.
Hayes GL. 1944. A method of measuring rainfall on windy slopes. *Monthly Weather Review* **72**(5): 111-114.
Hovind EL. 1965. Precipitation distribution around a windy mountain peak. *Journal of Geophysical Research* **70**(14): 3271-3278
Hutchinson P. 1970. A contribution to the problem of spacing raingages in rugged terrain. *Journal of Hydrology* **12**: 1-14.
James JW. 1964. The effect of wind on precipitation catch over a small hill. *Journal of Geophysical Research* **69**(12): 2521-2524.
Jungerius PD, Dekker LW. 1990. Water erosion in the dunes. *Catena Supplement* **18**: 185-193.
Jungerius PD, Verheggen AJT, Wiggers AJ. 1981. The development of blowouts in De Blink, a coastal dune area near Noordwijkerout, The Netherlands. *Earth Surface Processes and Landforms* **6**: 375-396.
Kim SE, Choudhury D, Patel B. 1997. Computations of complex turbulent flows using the commercial code FLUENT. *Proceedings of the ICASE/LaRC/AFOSR. Symposium on Modelling Complex Turbulent Flows*, Hampton, Virginia.
Kim SE, Choudhury D. 1995. A near-wall treatment using wall functions sensitized to pressure gradient. *ASME FED Vol. 217, Separated and Complex Flows.*
Lacy RE. 1951. Distribution of rainfall round a house. *Meteorological Magazine* **80**: 184-189.
Lal R, Lawson TL, Anastase AH. 1980. Erosivity of tropical rains. In *Assessment of erosion*, De Boodt M, Gabriels D (eds). Wiley: Chichester, 143-151.

Lentz RD, Dowdy RH, Rust RH. 1995. Measuring wind and low-relief topographic effects on rainfall distribution. *Applied Engineering in Agriculture* **11**(2): 241-248.
Lyles L, Dickerson JD, Schmeidler NF. 1974. Soil detachment from clods by rainfall : effects of wind, mulch cover, and initial soil moisture. *Transactions of the ASAE* **17**: 697-700.
Lyles L, Disrud LA, Woodruff NP. 1969. Effects of soil physical properties, rainfall characteristics, and wind velocity on clod disintegration by simulated rainfall. *Soil Science Society of America Proceedings* **33**: 302-306.
Lyles L. 1977. Soil detachment and aggregate disintegration by wind-driven rain. *SCSA Special Publication* **21**: 152-159.
McManus P, Jones A. 1994. Role of wind-driven rain, aerosols, and contaminated budwood in incidence and spatial pattern of fire blight in an apple nursery. *Plant Disease* **11**: 1059-1066.
Moeyersons J, De Ploey J. 1976. Quantitative data on splash erosion, simulated on unvegetated slopes. *Zeitschrift fur Geomorphologie* **25**: 120-131.
Moeyersons J. 1983. Measurements of splash-saltation fluxes under oblique rain. *Catena Supplement* **4**: 19-31.
Morsi SA, Alexander AJ. 1972. An investigation of particle trajectories in two-phase flow systems. *Journal of Fluid Mechanics* **55**(2): 193-208.
Moss WD, Baker S. 1980. Re-circulating flows associated with two-dimensional steps. *Aeronautical Quarterly* **31**: 151-172.
Pagliuca S. 1934. The measurement of precipitation on a windy Mountain Summit. *Transactions AGU*: 385-389.
Panofsky HA, Dutton JA. 1984. *Atmospheric turbulence*. John Wiley & Sons. New York; 397.
Phillips JFV. 1926. Rainfall interception by plants. *Nature*, December 11, 837-838.
Phillips JFV. 1928. Rainfall interception by plants. *Nature*, March 10, 354-355.
Poesen J. 1985. An improved splash transport model. *Zeitschrift fur Geomorphologie Neue Folge* **29**(2): 193-211.
Poesen J. 1986. Field measurements of splash erosion to validate a splash transport model. *Zeitschrift fur Geomorphologie Neue Folge, Suppl.-Bd.* **58**: 81-91.
Poesen J. 1988. Surface sealing on sandy and loamy soils: some aspects of seal formation and the influence of sealing on water erosion subprocesses. *Quaderni di Scienza del Suolo* **1**: 9-20.
Poreh M, Mechrez E. 1984. The combined effect of wind and topography on rainfall distribution. *Journal of Hydrology* **72**(1-2): 1-23.
Reid I. 1973. The influence of slope aspect on precipitation receipt. *Weather* **28**: 490-494.
Sache I. 2000. Short-distance dispersal of wheat rust spores by wind and rain. *Agronomie* **20**: 757-767.
Sandsborg J. 1970. The effect of wind on the precipitation distribution over a hillock. *Nordic Hydrology* **4**: 235-244.
Sharon D, Adar E, Lieberman G. 1983. Observations on the differential hydrological and/or erosional response of opposite-lying slopes, as related to incident rainfall. *Israel Journal of Earth-Sciences* **32**: 71-74.
Sharon D, Arazi A. 1997. The distribution of wind-driven rain in a small valley: an empirical basis for numerical model verification. *Journal of Hydrology* **201**: 21-48.
Sharon D, Morin J, Moshe Y. 1988. Micro-topographical variations of rainfall incident on ridges of a cultivated field. *Transactions of the ASAE* **31**(6): 1715-1722.
Sharon D. 1970. Topography-conditioned variations in rainfall as related to the runoff contributing areas in a small watershed. *Israel Journal of Earth-Sciences* **19**: 85-89.
Sharon D. 1980. The distribution of hydrologically effective rainfall incident on sloping ground. *Journal of Hydrology* **46**: 165-188.
Shih TH, Liou WW, Shabbir A, Zhu J. 1995. A new k-ε eddy-viscosity model for high Reynolds number turbulent flows – model development and validation. *Computers and Fluids* **24**(3): 227-238.
Van Dijk PM, Stroosnijder L, De Lima JLMP. 1996. The influence of rainfall on transport of beach sand by wind. *Earth Surface Processes and Landforms* **21**: 341-352.
Van Heerden WM. 1964. *Splash erosion as affected by the angle of incidence of raindrop impact*. PhD thesis, Purdue University, Lafayette, USA.
Wieringa J. 1992. Updating the Davenport roughness classification. *Journal of Wind Engineering and Industrial Aerodynamics* **41-44**: 357-368.

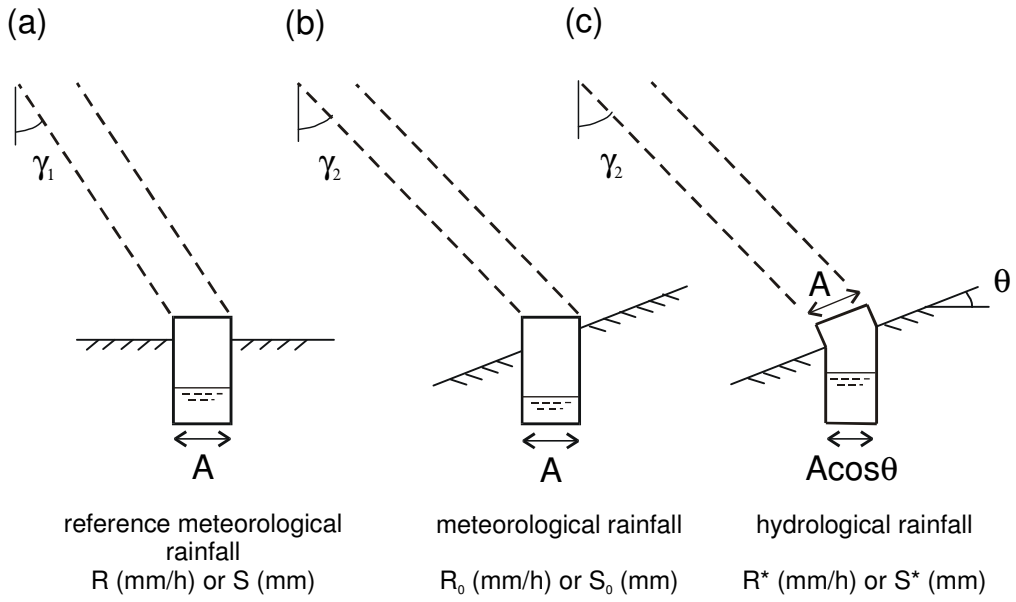


Fig. 1. Definition of (a) reference meteorological rainfall, (b) meteorological rainfall and (c) hydrological rainfall. R = rainfall rate, S = rainfall sum. $\gamma_1$ is the angle of the raindrop trajectories in an air-flow over flat topography far away from any obstructions. $\gamma_2$ is a local trajectory angle that is different from $\gamma_1$ because of the disturbance of the local air-flow by the topographic relief.

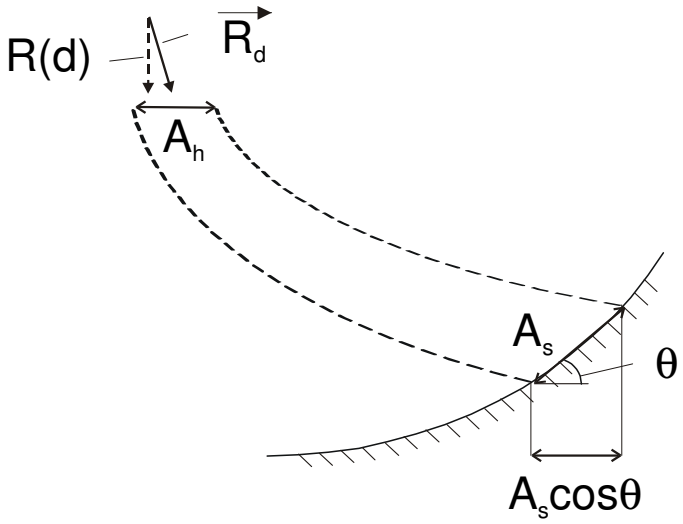


Fig. 2. Sketch illustrating the stream tube bounded by raindrop trajectories. The calculation of the specific catch ratio $\eta_d$ for raindrops with diameter d is based on conservation of mass for the raindrops in the stream tube. The vector $\overrightarrow{R_d}$ is the rain-intensity vector. Its flux through the surface $A_h$ is R(d) multiplied with $A_h$. This flux falls on the sloping soil surface $A_s$.

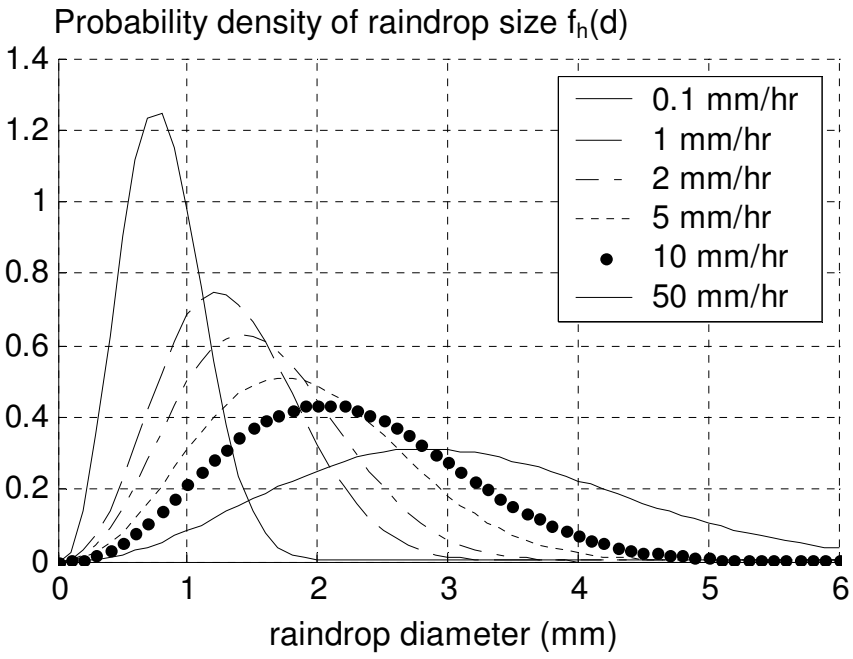


Fig. 3. Raindrop-size distribution through a horizontal plane with the reference rainfall intensity as a parameter – calculated from the raindrop-size distribution in a volume of air according to Best (1950).

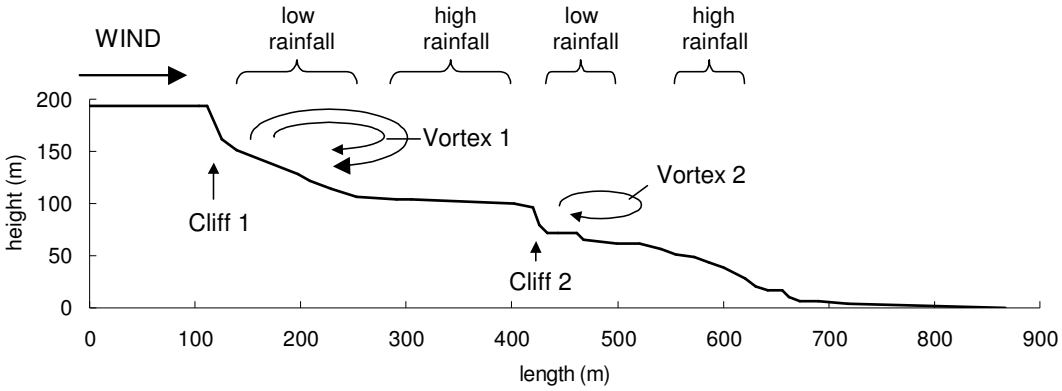


Fig. 4. Geometry of the steep irregular slopes with two major cliffs (east County Antrim, Northern Ireland). Craig (1980) suggested that vortices were formed in the lee of the cliff faces, as indicated, which he expected to be responsible for the uneven distribution of rainfall as indicated in the figure.

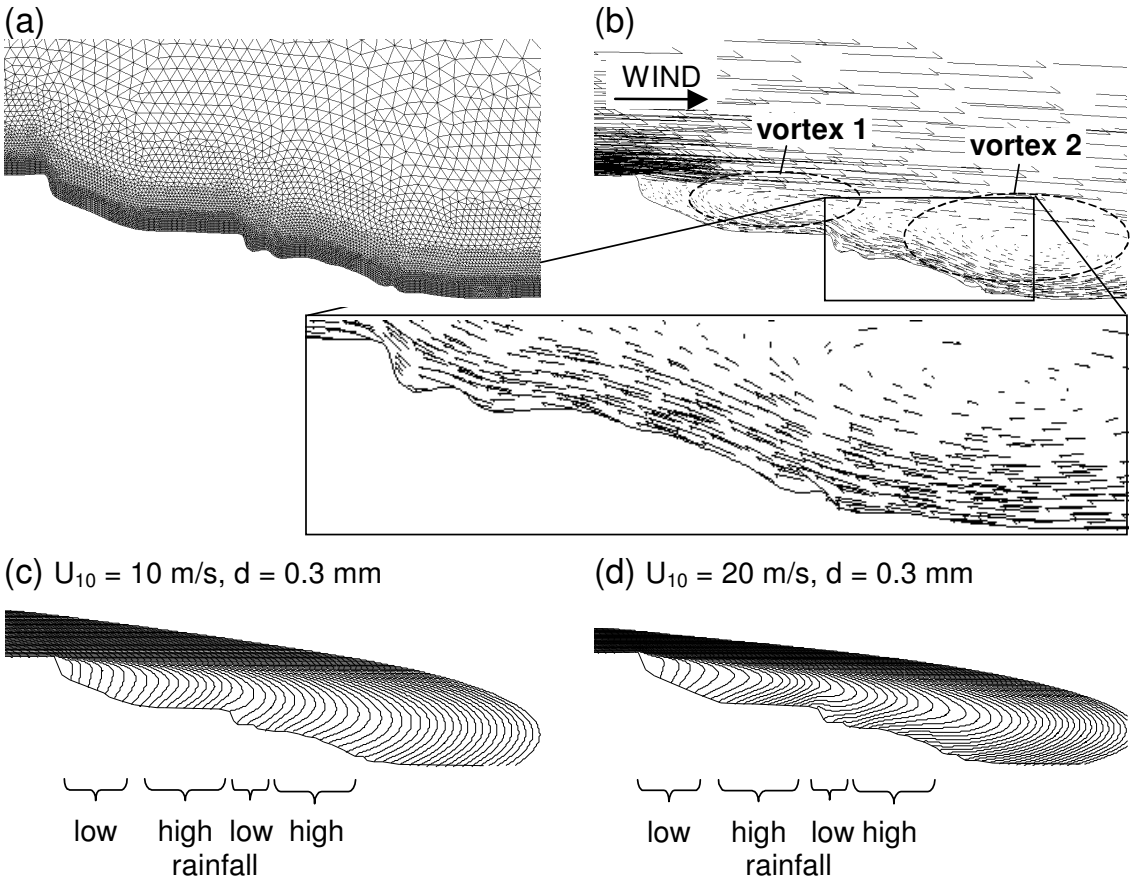


Fig. 5. Numerical simulation of wind-driven rain over the cliffs' area. (a) Part of the computational mesh, (b) Wind-flow pattern including two vortices, a smaller vortex 1 and a larger vortex 2, (c) Trajectories of 0.3 mm raindrops (drizzle) in the $U_{10}$ = 10 m/s flow field, (d) As (c) but in the $U_{10}$ = 20 m/s flow field.

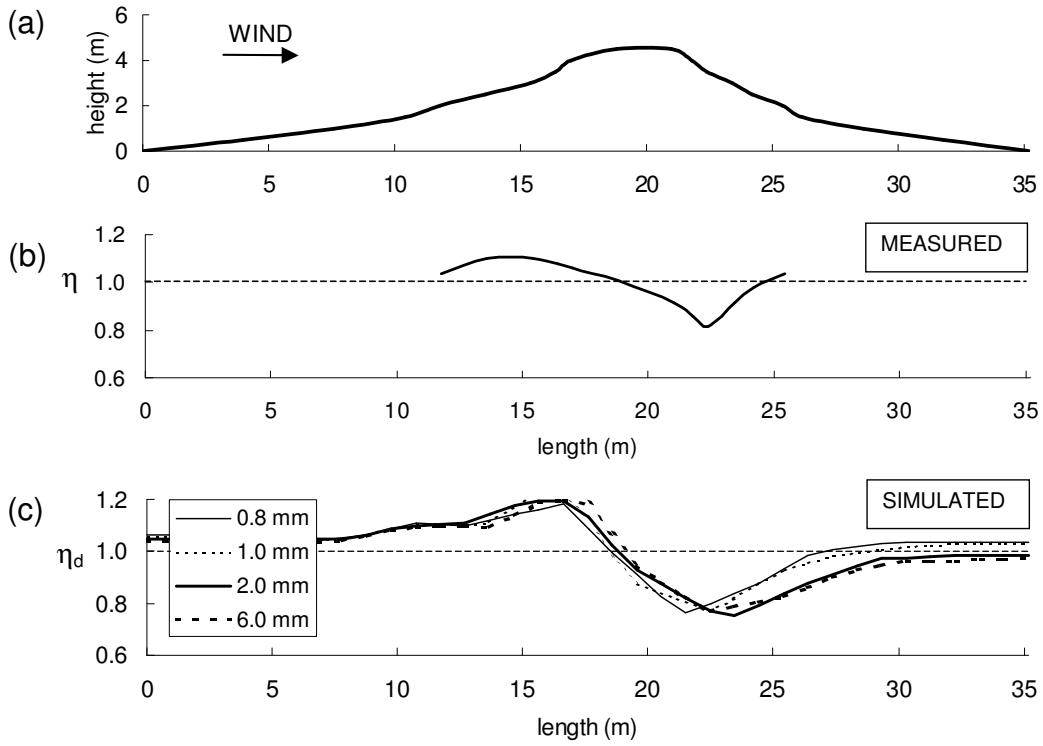


Fig. 6. (a) A SSW-NNE oriented transect of the small isolated hill studied by Sandsborg (1970). (b) Measured catch ratio η (hydrological rainfall sum divided by reference rainfall sum) along the transect. (c) Simulated profile of the specific catch ratio $\eta_d$ along the transect for several raindrop diameters.

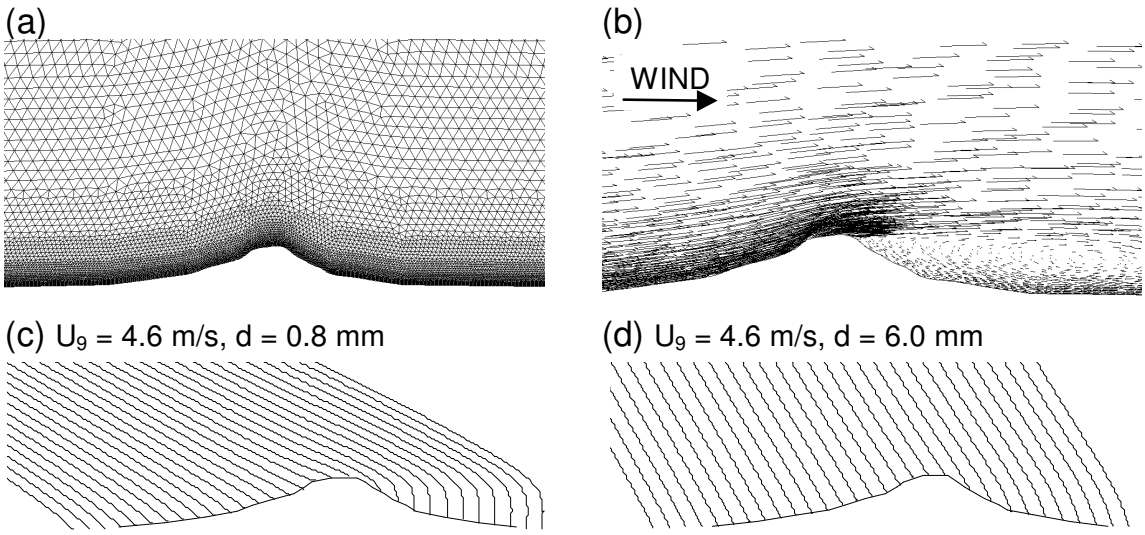


Fig. 7. Numerical simulation of wind-driven rain over the small hill. (a) Part of the computational mesh, (b) Wind-flow pattern, (c) Trajectories of 0.8 mm raindrops in the $U_9$ = 4.6 m/s wind-flow pattern, (d) As (c) but for 6.0 mm drops.

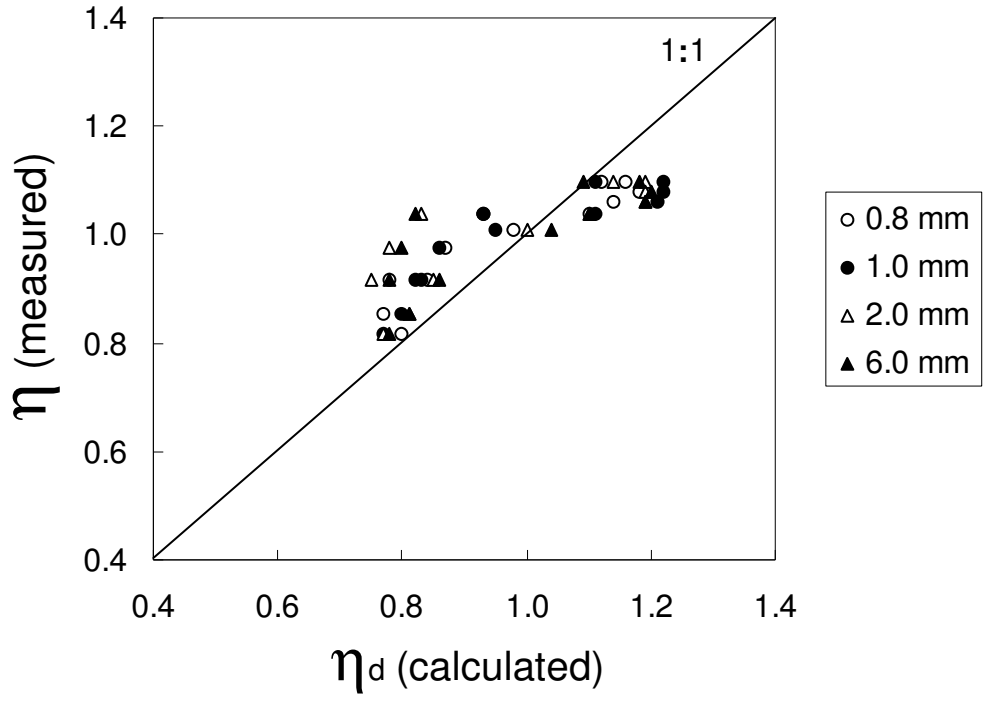


Fig. 8. Comparison of calculated specific catch ratio $\eta_d$ (for different raindrop diameters) and measured catch ratio $\eta$ at different positions along the transect of the small hill.

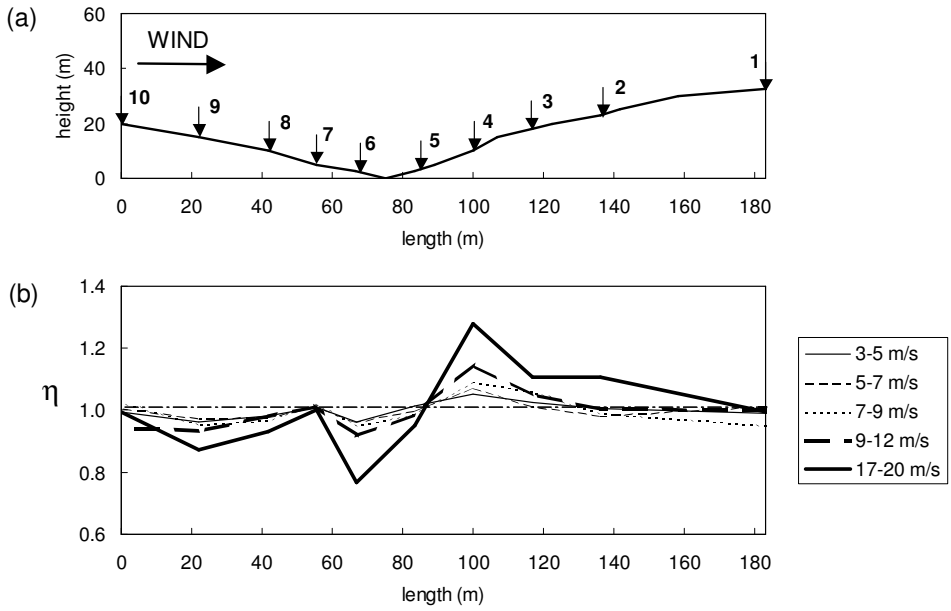


Fig. 9. (a) Geometry of a W-E oriented transect through the small valley Lehavim-N. The location and numbers of the rain gauges are indicated by the arrows. (b) Measured catch ratios (η) for different wind-speed classes.

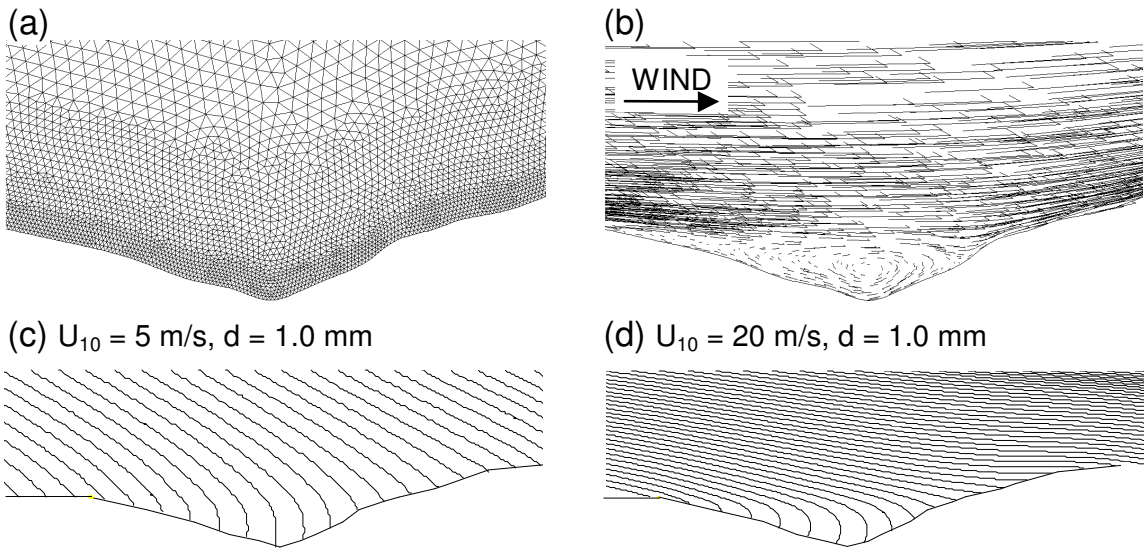


Fig. 10. Numerical simulation of wind-driven rain over the Lehavim-N transect. (a) Part of the computational mesh, (b) Wind-flow pattern with vortex at the bottom of the valley, (c) Trajectories of 1.0 mm raindrops in the $U_{10}$ = 5 m/s flow field, (d) As (c) but for the $U_{10}$ = 20 m/s flow field.

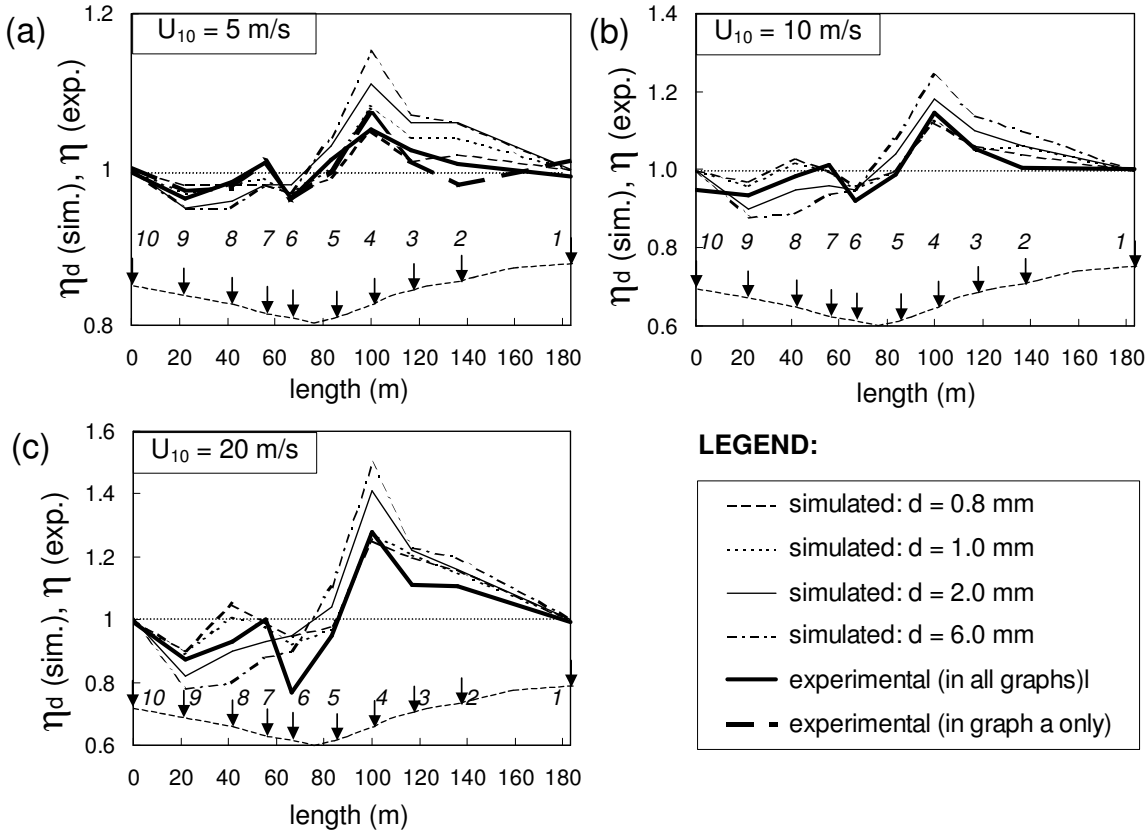


Fig. 11. Comparison of the calculated specific catch ratio $\eta_d$ (simulated) for four raindrop diameters with the measured catch ratio $\eta$ (experimental). (a) Calculation with $U_{10}$ = 5 m/s, measurements for wind speed classes $U_{10}$ = 3-5 m/s (thick solid line) and 5-7 m/s (thick dashed line). (b) Calc. with $U_{10}$ = 10 m/s, meas. for $U_{10}$ = 9-12 m/s (thick solid line), (c) Calc. with $U_{10}$ = 20 m/s, meas. for $U_{10}$ = 17-20 m/s (thick solid line).

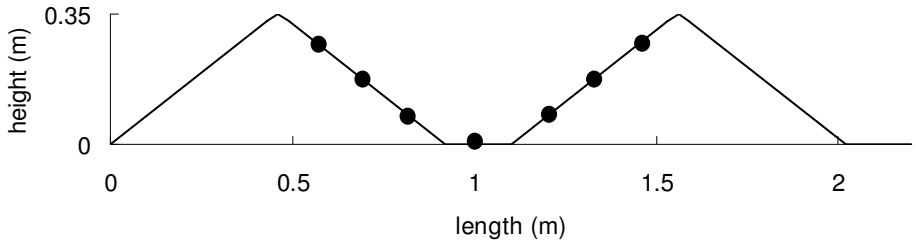


Fig. 12. Geometry of a transect of two ridges. The black dots indicate the positions where hydrological rainfall measurements were made by Sharon et al. (1988).

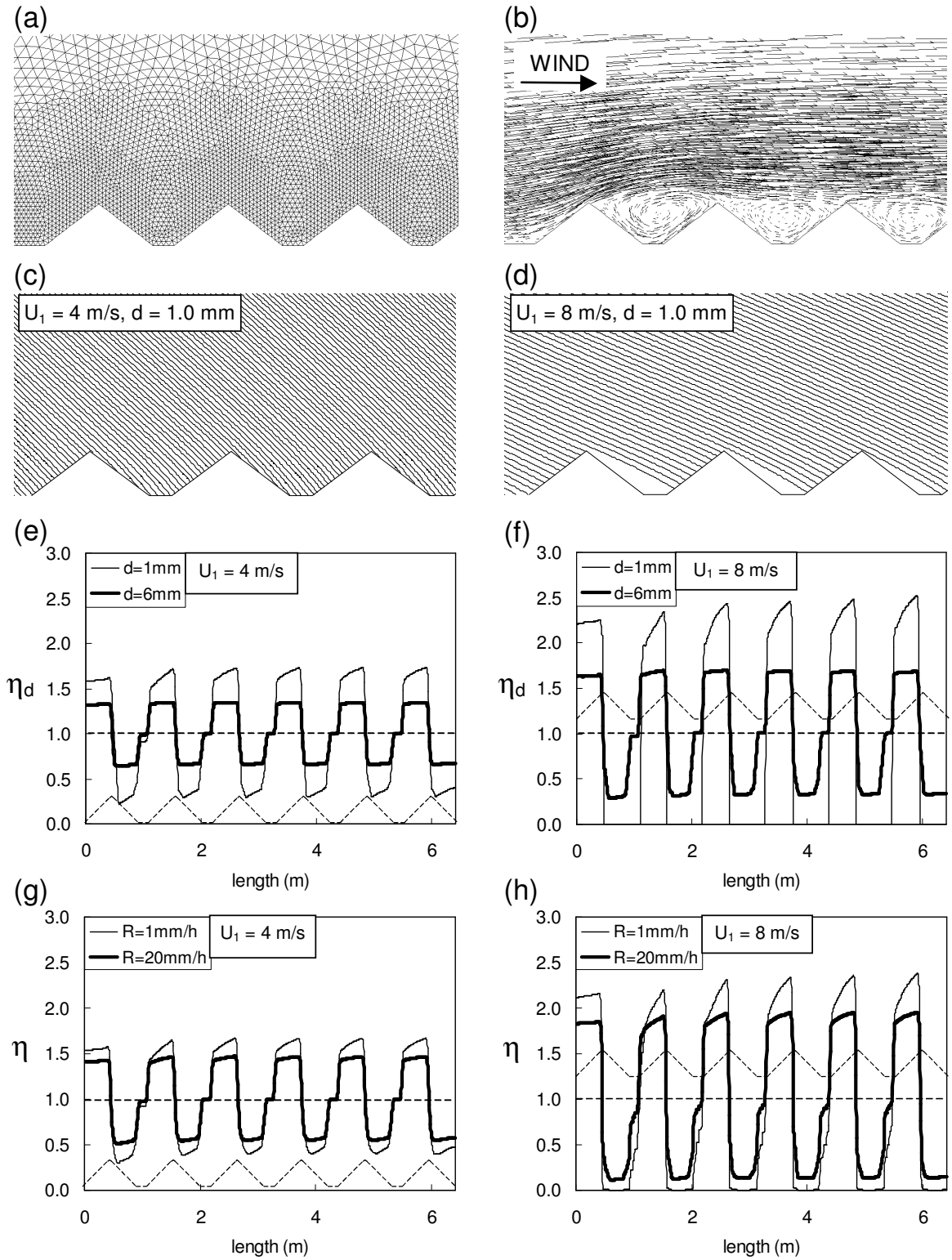


Fig. 13. Numerical simulation of wind-driven rain over a succession of six ridges. (a) Part of the computational mesh, (b) Wind-flow pattern over the first three ridges, (c) Trajectories of 1.0 mm raindrops in the $U_1$ = 4 m/s flow field for the first three ridges, (d) As (c) but for the $U_1$ = 8 m/s flow field, (e-f) Distribution of the specific catch ratio $\eta_d$ over the six ridges, (g-h) Same as (e-f) but for the catch ratio $\eta$.

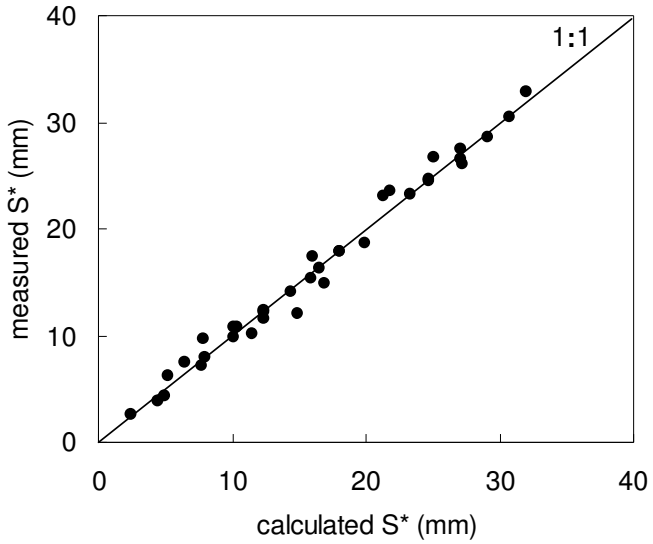


Fig. 14. Comparison of calculated and measured hydrological rainfall sum S* impacting the ridges at various positions for different storms.

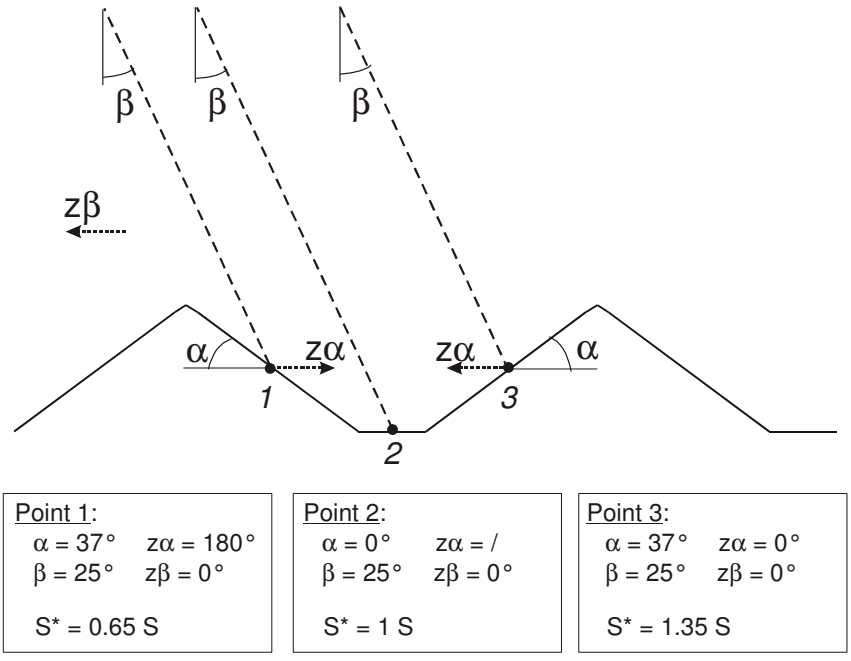


Fig. 15. Illustration of the application of the trigonometric formula (Eq. 7) for three points on the geometry. This formula assumes that the raindrop trajectories (dashed lines) are straight lines with the same angle β and it applies to each point of the geometry. zβ is the direction from which the rain is coming (e.g. north = 0°). zα is the aspect of the sloping soil surface at the point and α is the inclination of the slope at that point. The formula is applied for the example values given in the figure, yielding the relation between the hydrological rainfall amount S* and the reference meteorological rainfall amount S.

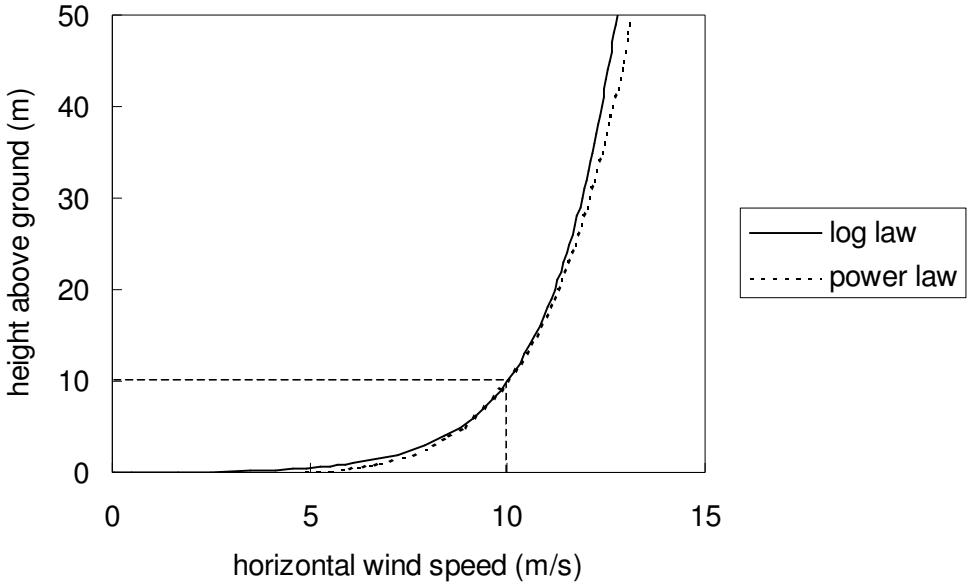


Fig. B.1. The logarithmic law and the power law for describing the increase of the mean horizontal wind speed with height in the atmospheric-boundary-layer flow over uniformly rough terrain. Both laws are matched at y = 10 m. ($U_{ref}$ = 10 m/s, $y_{ref}$ = 10 m, $y_0$ = 0.03 m, u* = 0.69 m/s, $\alpha_P$ = 0.17).

Table 1. Storm data as reported by Sharon et al. (1988). The residual percentage of rainfall for which no information is given in the table occurred with variable wind from other directions.

| storm no. | total rainfall S (mm) | % of total rain (%) | rain intensity (mm/h) | wind speed (m/s) | wind direction (° from N) |
|---|---|---|---|---|---|
| 9 | 6.4 | 18 | 6 | 14 | 230-235 |
| | | 70 | 11 | 7 | 260-265 |
| 12 | 24.7 | 10 | 2-3 | 3-5 | 180 |
| | | 65 | 3-6 | 3-6 | 200-225 |
| | | 23 | 6 | 1.5-4.5 | 330-030 |
| 13 | 27.0 | 30 | 6 | 5-5.5 | 45-65 |
| | | 46 | 3-7 | 4 | 195-215 |
| | | 23 | 7-11 | 4-6 | 250 |
| 14 | 12.3 | 75 | 4-6 | 3-5 | 165 |
| | | 10 | 3 | 2.5 | 155 |
| 15 | 10.0 | 90 | 13-20 | 5-8 | 295-300 |
| 16 | 18.0 | 5 | 10-13 | 3-5 | 190-220 |
| | | 18 | 2-18 | 4-9 | 240-255 |
| | | 23 | 9-12 | 2.5-5 | 280-320 |

Table 2. Hydrological rainfall measurements at the end of storm 9 for NE-SW and SE-NW transects as provided by Sharon et al. (1988). zα indicates the aspect (azimuth) of the ridge slope (degrees from north).

| Hydrological rainfall amounts (mm) | | | | | | |
|---|---|---|---|---|---|---|
| | NE-SW transect | | | SE-NW transect | | |
| | slope zα = 50° | bottom | slope zα = 230° | slope zα = 145° | bottom | slope zα = 325° |
| storm 9 | 2.6 | 6.3 | 10.3 | 4.4 | 7.5 | 8.1 |

Table 3. Comparison of calculated and measured hydrological rainfall sum on the ridges.

| Hydrological rainfall amounts (mm) | | | | | | | |
|---|---|---|---|---|---|---|---|
| | | NE-SW transect | | | SE-NW transect | | |
| | | slope zα = 50° | bottom | slope zα = 230° | slope zα = 145° | bottom | slope zα = 325° |
| storm 9 | calculated | 2.4 | 5.2 | 11.4 | 4.9 | 6.4 | 7.9 |
| | *measured* | *2.6* | *6.3* | *10.3* | *4.4* | *7.5* | *8.1* |
| storm 12 | calculated | 16.5 | 24.7 | 32.0 | 27.2 | 24.7 | 21.8 |
| | *measured* | *16.4* | *24.8* | *32.9* | *26.2* | *24.6* | *23.6* |
| storm 13 | calculated | 23.3 | 27.0 | 30.7 | 29.0 | 27.0 | 25.0 |
| | *measured* | *23.3* | *26.6* | *30.5* | *28.6* | *27.6* | *26.7* |
| storm 14 | calculated | 10.3 | 12.3 | 14.3 | 16.9 | 12.3 | 7.8 |
| | *measured* | *10.8* | *11.7* | *14.1* | *14.9* | *12.4* | *9.7* |
| storm 15 | calculated | 7.7 | 10.0 | 12.3 | 4.4 | 10.0 | 15.9 |
| | *measured* | *7.3* | *10.0* | *12.3* | *3.9* | *10.8* | *15.4* |
| storm 16 | calculated | 14.8 | 18.0 | 21.3 | 16.0 | 18.0 | 19.9 |
| | *measured* | *12.2* | *18.0* | *23.2* | *17.5* | *18.0* | *18.8* |

Table A.1. Davenport classification of effective terrain roughness as updated by Wieringa (1992). Values can be extracted from the table by a determination of the roughness class (landscape description) on condition that it is based on a fetch of at least 5 km.

| | $y_0$ (m) | Landscape description |
|---|---|---|
| 1 | 0.0002<br>Sea | Open sea or lake (irrespective of the wave size), tidal flat, snow-covered flat plain, featureless desert, tarmac, concrete, with a free fetch of several kilometres. |
| 2 | 0.005<br>Smooth | Featureless land surface without any noticeable obstacles and with negligible vegetation; e.g. beaches, pack ice without large ridges, morass, and snow-covered or fallow open country. |
| 3 | 0.03<br>Open | Level country with low vegetation (e.g. grass) and isolated obstacles with separations of at least 50 obstacle heights; e.g. grazing land without windbreaks, heather, moor and tundra, runway area of airports. |
| 4 | 0.10<br>Roughly open | Cultivated area with regular cover of low crops, or moderately open country with occasional obstacles (e.g. low hedges, single rows of trees, isolated farms) at relative horizontal distances of at least 20 obstacle heights. |
| 5 | 0.25<br>Rough | Recently-developed “young” landscape with high crops or crops of varying height, and scattered obstacles (e.g. dense shelterbelts, vineyards) at relative distances of about 15 obstacle heights. |
| 6 | 0.50<br>Very rough | “Old” cultivated landscape with many rather large obstacle groups (large farms, clumps of forest) separated by open spaces of about 10 obstacle heights. Also low large vegetation with small interspaces such as bush land, orchards, young densely-planted forest. |
| 7 | 1.0<br>Closed | Landscape totally and quite regularly covered with similar-size large obstacles, with open spaces comparable to the obstacle heights; e.g. mature regular forests, homogeneous cities or villages. |
| 8 | ≥ 2.0<br>Chaotic | Centres of large towns with mixture of low-rise and high-rise buildings. Also irregular large forests with many clearings. |

Table B.1. Calculation of the hydrological rainfall sum S* on NE-SW and SE-NW transects for storm 9.

a) Storm data (total rainfall sum S = 6.4 mm)

| storm part no. (-) | % of total rain (%) | rainfall sum S (mm) | rain intensity R (mm/h) | wind speed (m/s) | wind direction (° from N) |
|---|---|---|---|---|---|
| 1 | 18 | 1.15 | 6 | 14.0 | 230-235 |
| 2 | 70 | 4.48 | 11 | 7.0 | 260-265 |
| 3 | 12 | 0.77 | - | - | (var.) |

b) Calculation for NE-SW transect (50°/230°)

| storm part no. (-) | wind. sp. projected NE-SW (m/s) | η NE slope zα = 50° (-) | η bottom (-) | η SW slope zα = 230° (-) | S* NE slope zα = 50° (mm) | S* bottom (mm) | S* SW slope zα = 230° (mm) |
|---|---|---|---|---|---|---|---|
| 1 | 13.99 | 0.00 | 0.00 | 2.80 | 0.0 | 0.0 | 3.2 |
| 2 | 5.90 | 0.36 | 1.00 | 1.66 | 1.6 | 4.5 | 7.4 |
| 3 | - | 1.00 | 1.00 | 1.00 | 0.8 | 0.8 | 0.8 |
| | | | | **S* calc.** | **2.4** | **5.2** | **11.4** |
| | | | | **S* meas.** | **2.6** | **6.3** | **10.3** |

c) Calculation for SE-NW transect (145°/325°)

| storm part no. (-) | wind. sp. projected SE-NW (m/s) | η SE slope zα = 145° (-) | η bottom (-) | η NW slope zα = 325° (-) | S* SE slope zα = 145° (mm) | S* bottom (mm) | S* NW slope zα = 325° (mm) |
|---|---|---|---|---|---|---|---|
| 1 | 0.61 | 1.07 | 1.00 | 0.93 | 1.2 | 1.2 | 1.1 |
| 2 | 3.23 | 0.64 | 1.00 | 1.35 | 2.9 | 4.5 | 6.0 |
| 3 | - | 1.00 | 1.00 | 1.00 | 0.8 | 0.8 | 0.8 |
| | | | | **S* calc.** | **4.9** | **6.4** | **7.9** |
| | | | | **S* meas.** | **4.4** | **7.5** | **8.1** |